The mechanism of defect induced hydroxylation on pyrite surfaces and implications for hydroxyl radical generation in prebiotic chemistry

Article *in* Geochimica et Cosmochimica Acta · October 2018

DOI: 10.1016/j.gca.2018.10.009

CITATIONS
5

READS
223

10 authors, including:

Haiyang Xian
Chinese Academy of Sciences
22 PUBLICATIONS **110** CITATIONS
SEE PROFILE

Jian-xi Zhu
Chinese Academy of Sciences
226 PUBLICATIONS **5,832** CITATIONS
SEE PROFILE

Wei Tan
Chinese Academy of Sciences
27 PUBLICATIONS **313** CITATIONS
SEE PROFILE

Hongmei Tang
Chinese Academy of Sciences
6 PUBLICATIONS **17** CITATIONS
SEE PROFILE

Available online at www.sciencedirect.com

ScienceDirect

Geochimica et Cosmochimica Acta 244 (2019) 163–172

Geochimica et Cosmochimica Acta

www.elsevier.com/locate/gca

The mechanism of defect induced hydroxylation on pyrite surfaces and implications for hydroxyl radical generation in prebiotic chemistry

Haiyang Xian [a,b], Jianxi Zhu [a,*], Wei Tan [a], Hongmei Tang [a,b], Peng Liu [a,b] Runliang Zhu [a], Xiaoliang Liang [a], Jingming Wei [a,b], Hongping He [a,b], H. Henry Teng [c,*]

[a] *CAS Key Laboratory of Mineralogy and Metallogeny & Guangdong Provincial Key Laboratory of Mineral Physics and Materials, Guangzhou Institute of Geochemistry, Chinese Academy of Sciences (CAS), Guangzhou 510640, China*

[b] *University of Chinese Academy of Sciences, Beijing 100049, China*

[c] *Institute of Surface-Earth System Science, Tianjin University, Tianjin 300072, China*

Received 30 March 2018; accepted in revised form 7 October 2018; Available online 13 October 2018

Abstract

The generation of reactive oxygen species H_2O_2 and OH· from pyrite in anaerobic environments plays an important role in the evolution of early Earth. What remains debatable is the underlying mechanism leading to the OH· generation reactions. Using a comprehensive approach combining X-ray photoelectron spectroscopy and *ab initio* calculations, we investigated binding energies and valence band structures of defective pyrite surfaces in an attempt to interrogate pyrite-mediated H_2O dissociation in the presence and absence of crystal defects. The results show that, while energetically inhibited on perfect crystal faces, H_2O dissociation is thermodynamically favored at defective sites. Furthermore, the formation of surface defects can lead to an energy shift in valence bands and thereby forming two defect states. Simultaneously, interaction between both defect states and water molecules makes the hydroxylation energetically favored on the pyrite surface. The hydroxylation occurs through proton transfer from water to a defective S monomer, resulting in an ≡Fe—O(H)···H—S≡ structure. These findings provide new insight into pyrite-assisted OH· formation processes in anaerobic conditions and may be important for understanding prebiotic chemistry and the evolution of early Earth.

Keywords: Pyrite surfaces; Hydroxylation; Defects; Valence band; Hydroxy radical; Prebiotic chemistry

1. INTRODUCTION

The formation of reactive oxygen species (ROS), H_2O_2 and OH· in particular, in anaerobic environments has been proposed to be a driving force for the anaerobic photosynthetic transformation process in prebiotic synthesis, and hence, may have aided the origin and evolution of life on Earth (McKay and Hartman, 1991; Awramik, 1992; Blankenship and Hartman, 1998; Schoonen et al., 2004). Further, the combination of two OH· can produce H_2O_2 and subsequently O_2, constituting a potential pathway for the oxygen generation and accumulation on early Earth (Borda et al., 2001). In both cases, ROS may have played a critical role in the early history of the Earth.

Despite the biochemical evidence indicating the significant role of OH· in the development of prebiotic organisms

* Corresponding authors.
E-mail addresses: zhujx@gig.ac.cn (J. Zhu), hteng@gwu.edu (H.H. Teng).

https://doi.org/10.1016/j.gca.2018.10.009
0016-7037/

(Blankenship and Hartman, 1998), it remains unclear how OH· formed through an abiotic approach in anaerobic environments. Previously, the formation process was attributed to photochemical reactions in CO_2-dominated atmosphere (Kasting and Pollack, 1984). However, later work (Kasting et al., 1989; Borda et al., 2001) suggested that this photochemical model is not robust enough to generate high H_2O_2 concentrations. It was then proposed that pyrite surfaces mediate H_2O_2 formation could become an acceptable pathway (Borda et al., 2001) because of the abundance of sulfide minerals on the surface of early Earth (Tian et al., 2005). Of all the sulfide minerals tested, studies have since (Borda et al., 2003; Kwan and Voelker, 2003; Garrido-Ramírez et al., 2010; Wang et al., 2012) shown that pyrite is the most efficient in terms of ROS generation through abiotic approach in anaerobic conditions and hence is termed the pyrite-only Fenton-like reagent (Wang et al., 2012).

Although it becomes increasingly clear that the species of OH· can indeed form at the pyrite-water interface in anaerobic environments (Borda et al., 2001; Cohn et al., 2004, 2010; Wang et al., 2012; Zhang et al., 2016), the underlying mechanism is still far from certain. Borda et al. (2003) proposed that, in O_2-free water, OH· is derived from the oxidation of H_2O by the defective Fe sites on the pyrite surface through:

$$\equiv Fe(III) + H_2O_{(ads)} \rightarrow \equiv Fe(II) + OH^{\cdot}_{(ads)} + H^+ \qquad (1)$$

While this pathway is consistent with the observation of OH· formation during the grinding of sulfide minerals in an anaerobic environment (Javadi et al., 2013; Javadi and Hanumantha, 2014), Buckley and Woods (2015) argued that reaction (1) is unlikely to be thermodynamically feasible. Ultimately, the reaction mechanisms remain to be clarified.

The purpose of the present study is to probe the effect of surface energetics on pyrite-mediated H_2O dissociation in the presence and absence of crystal defects. To achieve the goal, we performed experimental XPS valence band spectrum analyses and *ab initio* simulation to identify the valence band contributions of defects on pyrite {1 0 0} surfaces. Our results showed that Fe and S atoms at defect sites contribute significantly to the top of the valence band in comparison to pristine surfaces. Furthermore, we found that, while energetically inhibited on perfect crystal faces, H_2O dissociation is in fact thermodynamically favored at defective sites due to the reconfigured surface electronic structure.

2. MATERIAL AND METHODS

2.1. Experiments

Stock pyrite (from Navajun, La Rioja Province, Spain) chips with dimensions of $5 \times 5 \times 2$ mm^3 were cut from a cubic crystal and ultrasonically cleaned in ethanol for 30 min. Prior to experiments, the chips were chemically washed (Cabán-Acevedo et al., 2014) for 30 s in a mixed acid solution (48% HF, 70% HNO_3, and ≥99.99% acetic acid in a volume ratio of 1:2:1), ultrasonically rinsed in ethanol, and finally, dried by high purity N_2 gas.

The pyrite structure and surface orientation were determined by electron back-scattered diffraction (EBSD), as shown in Fig. 1. The EBSD pattern and the corresponding upper hemisphere pole projection figures validate the examined surface was from {1 0 0} faces. The chemical composition of the employed sample was characterized by an electro-probe microanalyzer (EPMA). The results indicated that the pyrite contains less than 0.5 wt% impurity elements, including Co, Ni, and Au, as shown in Table 1. Although the impurities may shift the electronic structure of natural pyrite (Abraitis et al., 2004), the effect of the impurity elements was omitted in the present study as we mainly focus on the valence band change after the formation of S vacancies. The X-ray photoemission spectra (XPS) were collected by a Thermo Scientific K-Alpha instrument (base pressure 10^{-8} mbar, Al Kα source at 1486.8 eV). The XPS spectrometer was equipped with an Ar^+ ion gun which can preferentially remove lighter elements over heavier ones (Cabán-Acevedo et al., 2014) through sputtering (S over Fe in the case of pyrite) to produce defects on the surface. In this study, a mild sputtering (1000 V Ar^+ beam at medium current) was performed for 20–180 s on the samples to generate an S-depleted defective surface. The XPS spectra of pristine and sputtered pyrite were collected before and 15-min after sputtering.

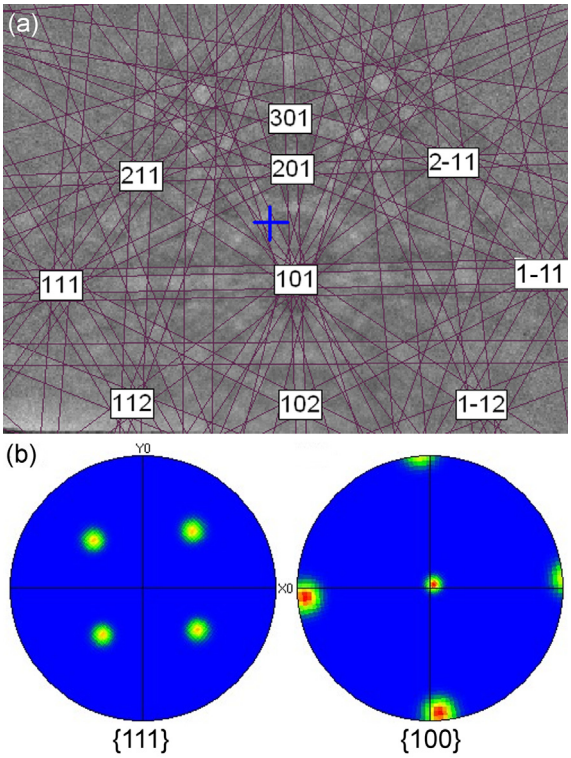

Fig. 1. EBSD pattern (a) and the crystallographic orientations plotted in upper hemisphere pole figures (b) of the natural cubic pyrite face.

Table 1
Elemental composition of the single pyrite crystals used in this study (wt%).

Elements	Fe	S	Co	Ni	Au
Percentage	46.394	53.282	0.232	0.071	0.017

2.2. Calculation details

All calculations were performed by the Vienna *Ab initio* Simulation Package (VASP) (Kresse and Furthmuller, 1996), which is based on the density functional theory (DFT), along with the projector augmented wave method (Kresse and Joubert, 1999). The PBE functions (Perdew et al., 1996) were utilized for the description of exchange-correlation interaction among electrons. The electron-ion interactions were included within a plane wave basis with an energy cutoff of 350 eV (Zhang et al., 2012) and a convergence of 10^{-6} eV. DFT + U, which was verified to be well suited for the description of pyrite (Zhang et al., 2012, 2015) and was adopted for the treatment of Fe 3d orbitals. A lattice constant of 5.423 Å and an indirect band gap of 0.95 eV for the bulk pyrite were obtained using a U-J parameter of 1.6 eV (Herbert et al., 2013), and they are in good agreement with published experimental data and previous calculations (Stevens et al., 1980; Ferrer et al., 1990; Kleppe and Jephcoat, 2004). Transition states were calculated by the climbing – nudged elastic band (CI-NEB) method implemented in VASP (Henkelman et al., 2000; Henkelman and Jónsson, 2000). The net charge distribution was treated by the Bader charge-division scheme based on the electronic charge density (Bader, 1990), which was emended in code developed by the Henkelman Group (Henkelman et al., 2006; Sanville et al., 2007; Tang et al., 2009). Although the Bader charge cannot be directly comparable to the chemical oxidation state, such as Fe(II) and Fe(III), the increase and decrease of the Bader charge can be used to represent the charge transfer between atoms in the considered models.

The pyrite FeS_2{1 0 0} surface was modeled by a periodic slab of seven FeS_2 layers (21 atomic layers). Individual slabs were separated by a sufficient vacuum (~17 Å). The geometry optimization of the defect-free surface was performed on a (1 × 1) unit cell and a Monkhorst-Pack mesh method (Monkhorst and Pack, 1976) with a 6 × 6 × 1k-point sampling within the Brillouin zone. A (2 × 2) supercell was employed for the geometry optimization of the defective surface and the electronic structure calculations. The slabs were constructed with identical surfaces to avoid artificial electric fields in the vacuum for studies of defective surfaces. All S atoms in the first FeS_2 layer were exposed to the vacuum. Two defective configurations with a surface S vacancy were considered (Fig. 2). The S_S, S_B, and S_M represent the surface dimer S, the bulk dimer S and the surface defective monomer S, respectively. The Fe_S, Fe_B, Fe_{S1} and Fe_{S2} represent the surface 5-fold Fe formed from the surface cleavage, the bulk 6-fold Fe, the surface 4-fold Fe bonded to surface S vacancy and the 5-fold Fe bonded to the surface S vacancy. In contrast, only one stable configuration (model A, Fig. 2) was observed to be a reasonable defective model for the pyrite {1 0 0} surface following geometry optimization. Both Fe and S atoms in the central layer were fixed at the corresponding bulk positions during the geometry optimization, whereas all other atoms were fully relaxed until forces became smaller than 0.02 eV/Å.

3. RESULTS

3.1. Energetics of hydroxylation on defective pyrite {1 0 0}

Compared to an ideal pyrite {1 0 0} surface, water dissociative adsorption is energetically favorable on defective surfaces (see Table 2). On the defective surface, the calculated adsorption energies of molecular and dissociative configurations (Fig. 3) are −63.68 and −70.42 kJ/mol, respectively. The Fe—O and S—H bond lengths are estimated to be 2.10–2.13 and 1.52 Å, respectively. From the most stable configurations, as shown in Fig. 3, we can observe that water interacts with one and two defective Fe sites for molecular and dissociative adsorption, respectively. Furthermore, ≡Fe—OH and ≡S—H were also observed in the dissociative configuration.

The minimum energy pathway for the water dissociation on the defective pyrite {1 0 0} surface (Fig. 4) shows two stages what contain a metastable configuration and two transition states. The activation energies of the two stages are 23.14 and 1.92 kJ/mol. The meta stable configuration shows that the water interacts with two defective Fe sites without dissociation. Therefore, water dissociation on defective pyrite {1 0 0} surfaces can be defined as two

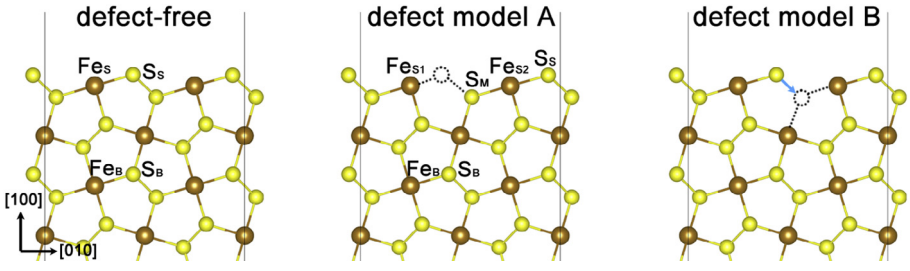

Fig. 2. Relaxed structure of defect-free and two defective pyrite {1 0 0} surface models (rendered by VESTA by Momma and Izumi, 2008). The light-yellow spheres represent S atoms; the brown spheres represent Fe atoms). (For interpretation of the references to colour in this figure legend, the reader is referred to the web version of this article.)

Table 2
Comparison of selected properties of an adsorbed water on ideal and defective pyrite {1 0 0} surfaces (bond lengths in Å and binding energies in kJ/mol).

Surface type	Adsorption type	Binding energy	d(Fe—O)	d(H—O)	d(S—H)	Reference
Ideal surface	Molecular	−54.14	2.12	0.10	–	Stirling et al. (2003)
		−52.68				
		−65.69	2.13	–	–	Sit et al. (2012)
		−56.19	2.11	–	–	Chen et al. (2014)
		−60.67	2.15	–	–	Dos Santos et al. (2016)
	Dissociative	+81.21	2.01	0.98	1.37	Stirling et al. (2003)
Defective surface	Molecular	−63.68	2.10	0.98	–	This study
	Dissociative	−70.42	2.12	0.98	1.52	This study
			2.13			

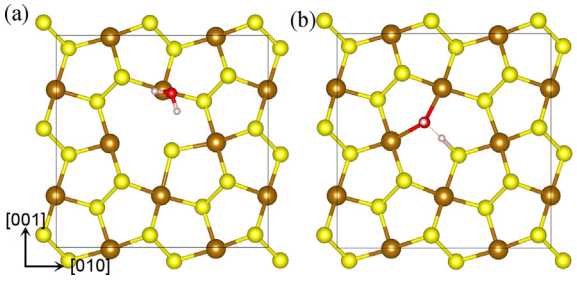

Fig. 3. Most stable water molecular (a) and dissociative (b) configurations, the relevant Fe—O, O—H, and S—H distances in Å on the defective pyrite {1 0 0} surface with an S vacancy.

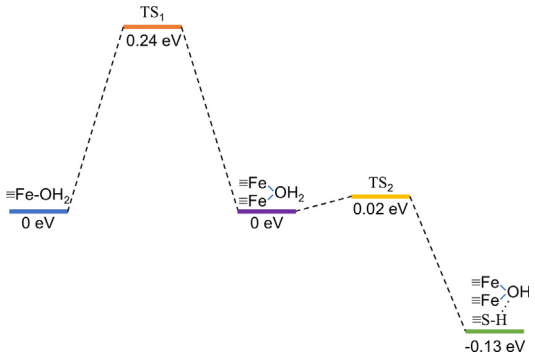

Fig. 4. Minimum energy pathway for the water dissociation on the defective pyrite {1 0 0} surface with an S vacancy.

stages: (1) interaction with defective Fe sites and (2) interaction with monomer S site and formation of S—H bond.

3.2. S 2*p* and Fe 2*p* spectra of defective pyrite surfaces

On pristine pyrite samples, bulk and surface S $2p_{3/2}$ bands were identified at the binding energy of 162.70 and 162.10 eV, each having its spin-orbit split $2p_{1/2}$ with energy approximately 1.20 eV higher in the S 2*p* spectra (Fig. 5a). The 0.6 eV shift between the bulk (S_B) and surface (S_S) S dimer was consistent with previous measurements by synchrotron XPS (Nesbitt et al., 2000; Andersson et al., 2004). The peak above the energy level of bulk and surface

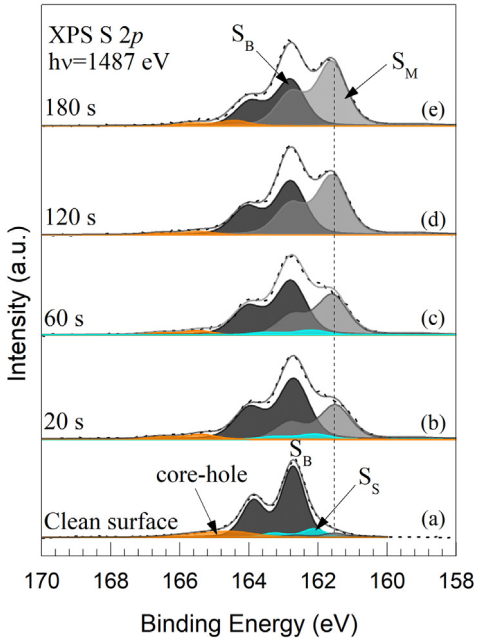

Fig. 5. S 2*p* X-ray photoemission spectra of acid washed clean pyrite {1 0 0} surface and surfaces following various durations of ion sputtering (20–180 s) (All peaks were fitted by doublets with a 1:0.51 ($2p_{3/2}$:$2p_{1/2}$) height ratio and with the same full width at half maximum (FWHM) in each spectrum).

S $2p_{3/2}$ bands was attributed to the core-hole effect (Herbert et al., 2014). No impurities, such as sulfate, were detected in the spectra, indicating the presence of residual oxidation product on the acid washed pyrite {1 0 0} surface was negligible to conventional XPS.

Upon sputtering, a new S $2p_{3/2}$ feature at binding energy 161.50 eV, i.e., 1.20 eV lower than that of bulk S $2p_{3/2}$, was observed (Fig. 5b, c, d, and e), consistent with what was reported after Ne^+-ion sputtering (Andersson et al., 2004, 2014) and hence signaled the presence of surface S monomers (S_M) (Andersson et al., 2004). As such, the locations of the lost S atoms become surface vacancies.

The sharp single peak at ~707.2 eV of the Fe 2*p* spectra (Fig. 6a) was assigned to the low-spin $2p_{3/2}$ Fe^{2+} bulk state. The tail on the high-energy side of the Fe $2p_{3/2}$ spectra was

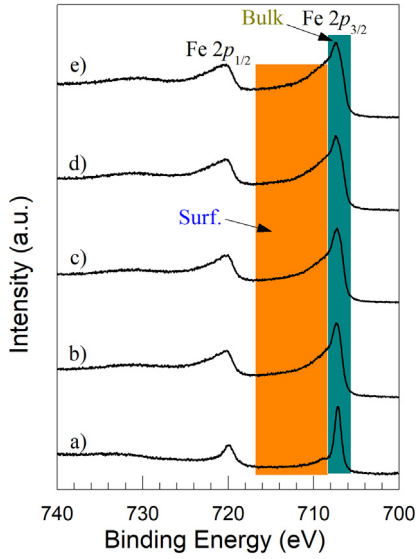

Fig. 6. Fe 2*p* X-ray photoemission spectra of acid washed pyrite {1 0 0} surface and surfaces following various durations of ion etching (20–180 s, corresponding to (a)–(e), respectively).

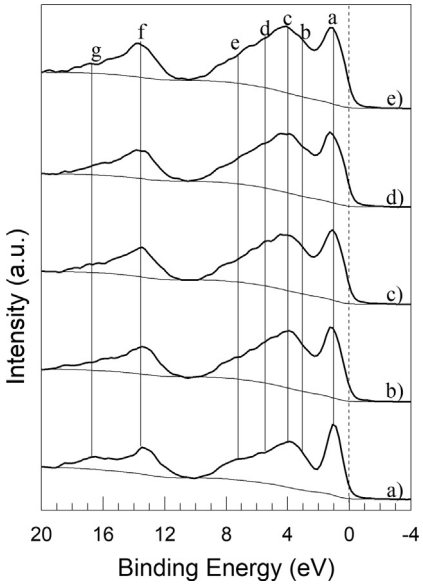

Fig. 7. XPS valence band spectra of acid washed clean pyrite {1 0 0} surface and surfaces following various durations (20–180 s, corresponding to a–e) of Ar^{+}-ion bombardment.

assigned to surface state (Nesbitt et al., 1998). Upon sputtering, the intensity of the surface tail features increased along the sputtering time (Fig. 6b, c, d, and e).

3.3. XPS valence band spectra of defective pyrite surfaces

Consistent with previous studies (Nesbitt et al., 2003), a typical valence band spectrum on the pristine pyrite surfaces consisted of seven contributions (Fig. 7a). Specifically, whereas peak "a" is the outmost feature of the valence band and contained orbital contributions from Fe-S π^{*} (molecular) and surface Fe 3*d*, the peaks "b" and "c" arise from the Fe-S π and Fe-S σ molecular orbitals, respectively. Moreover, the sets of peaks "d" and "e" as well as "f" and "g" were derived from the S-S 3*p* and S-S 3*s* atomic orbitals mixing, respectively.

This valence band pattern (Fig. 7b, c, d, and e) underwent noticeable change upon Ar^{+}-ion sputtering. For example, while the intensity of peak "a" was significantly stronger than that of "c" (Fig. 7a) on pristine surfaces, sputtering decreased the difference and ultimately made them quite similar (Fig. 7e). In addition, between peaks "f" and "g", it appeared that the sputtering effect was more pronounced on the former.

3.4. Calculated charge distribution on pyrite surface

The computed net charge (Fig. 8) on each atom of fully relaxed defect-free and defective model A, using the Bader charge-division scheme (Bader, 1990; Henkelman et al., 2006) is consistent with literature data (Zhang et al., 2012). More specifically, for defect-free models, surface Fe (+0.76 e) lost 0.1 electrons relative to the bulk Fe (+0.62 e), whereas the surface S (from −0.36 e to −0.37 e) gained approximately 0.05 electrons in comparison to the bulk counterpart (from −0.29 e to −0.31 e). The charge

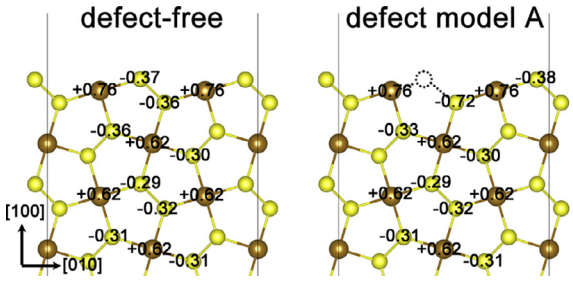

Fig. 8. Bader charge distribution of defect-free and defective pyrite {1 0 0} surface displayed in Fig. 1. Light yellow spheres represent S atoms; brown spheres represent Fe atoms. (For interpretation of the references to colour in this figure legend, the reader is referred to the web version of this article.)

distribution pattern in the defective model A was similar to the defect-free surface, except for the mono S atom where the charge (−0.72 e) exceeded more than twice of the bulk S atoms (−0.31 e).

3.5. Density of states (DOS) of defective pyrite surfaces

To further rationalize the XPS observations, DFT + U calculations were performed to comprehend the DOS for the defective configurations of pyrite. The projected DOS (Fig. 9) on atoms with different coordination numbers shows that the valence band mainly arises from the Fe 3*d* orbital and the S 3*p* orbital contributions. The DOS of surface and defective atoms showed more contribution to the top of the valence band. In specific, the peak at about −15 eV was absent in the DOS of S monomer while it was present in that of (bulk and surface) the S dimer.

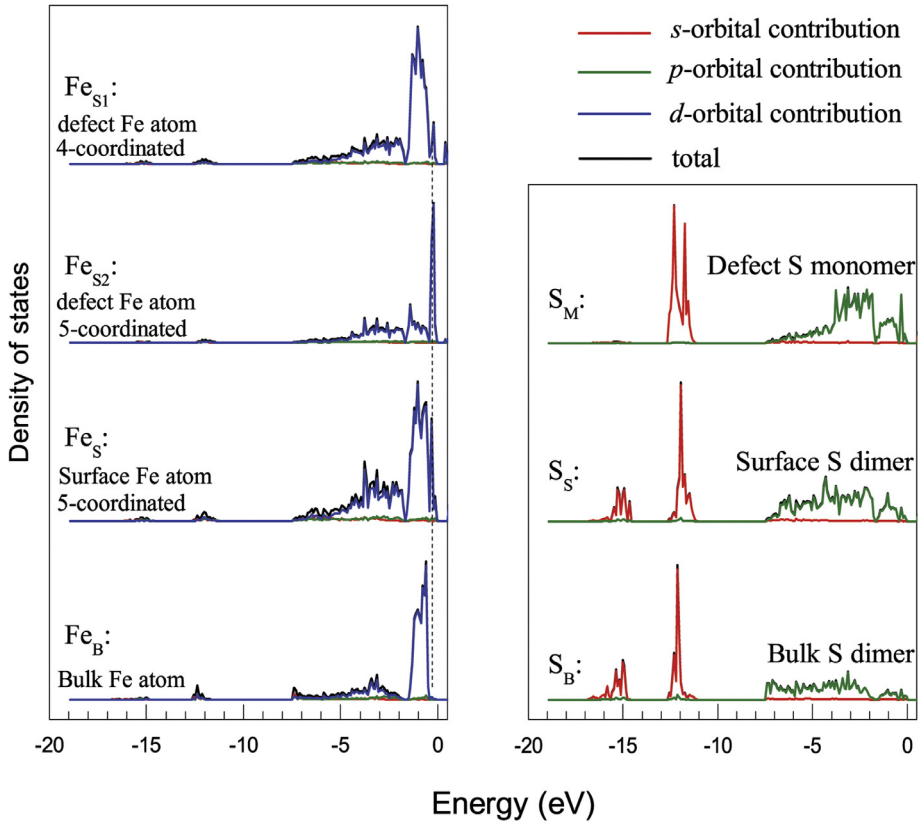

Fig. 9. Local density of states (LDOS) of various iron and sulfur atoms in defective pyrite.

4. DISCUSSION

We will discuss our results based on the following outline: (1) how the defects affect the energetics of its valence band and (2) how the energy offsets affect water dissociation, *i.e.*, hydroxylation, on pyrite surface. Therefore, we primarily examine the defects' contribution to valence bands and then discuss the hydroxylation on defective pyrite surfaces relative to the energy offsets in the valence band.

4.1. The consistency between experimental and theoretical data

The correlation between the experimental valence band spectra and the calculated DFT + U electronic structure could be assessed by the weighted density of states (WDOS) by using the experimental cross-section at the utilized photon energy (1487 eV), Gaussian smearing (0.25 eV), published atomic subshell (Yeh and Lindau, 1985), and a Shirley-type (Shirley, 1972) background removal. The results (Fig. 10) show a general agreement between the computed WDOS and the experimental XPS valence band spectra, indicating reasonableness of the defect model adopted in this work for interpreting the valence band spectra of defective pyrite {1 0 0} surfaces. The minor differences in peak shift could be explained by errors in the DFT + *U* calculations due to the approximate treatment employed.

4.2. Charge distribution on defective pyrite {1 0 0} surface

The underlying specific species of the tail features in Fe 2*p* spectra (Fig. 6) are uncertain (Schaufuss et al., 1998; Stirling et al., 2007). Nesbitt et al. (1998) assigned surface Fe^{3+} and Fe^{2+} to this tail based on the hypothesis of a redox reaction: Fe^{2+}(surf.) + S^{-} → Fe^{3+} (surf.) + S^{2-}(-surf.). However, previous *ab initio* calculations by Stirling et al.(2007) suggest that only surface Fe bonded to an adatom S could change from the Fe^{2+} to the Fe^{4+} state. The Bader charge of surface Fe (+0.76) and S (−0.37) are slightly larger and smaller than those of bulk Fe (+0.62) and S (−0.32), respectively, indicating charge transfer between the surface Fe and S atoms are of little consequence if there are S vacancies on the surface. However, the Bader charge of surface S is much higher than that of the S monomer (−0.72), indicating the oxidation state of surface S is between -1 and -2 states and the surface Fe is between +2 and +3 states. Thus, we define these states as the active surface states. To distinguish our results from previous viewpoint about the charge of the surface atoms, we assign the surface Fe atoms to +2.5 states and the surface S to −1.25 states.

Furthermore, the Bader charge analysis indicated that negligible electron transfer from Fe to S on defective surfaces took place, consistent with the conclusion from Stirling et al. (2007) and Sit et al. (2012), which may be caused by the employed physical models during first-

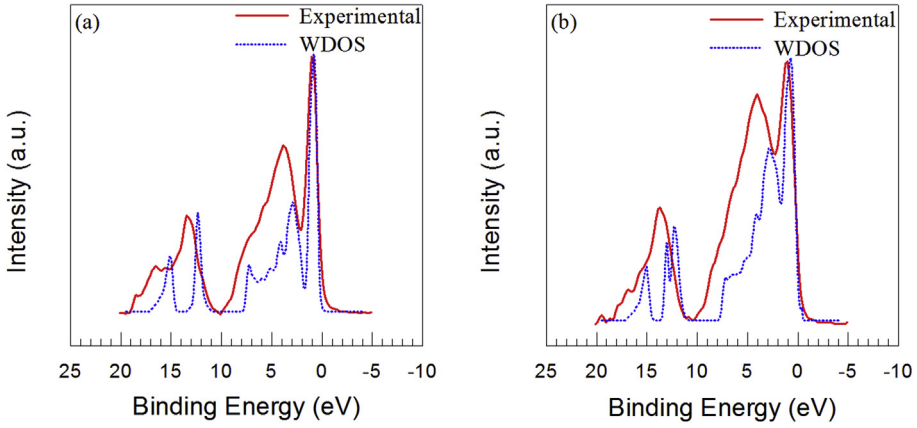

Fig. 10. The weighted density of state for defect-free (a) and defective (b) pyrite {1 0 0} surfaces compared to the experimental XPS valence band spectra (dotted line).

principles quantum mechanical calculations (Raebiger et al., 2008). In this regard, we conclude that the defective Fe atoms possess similar charge with the ideal surface Fe (+2.5). The Bader charge of monomer S was nearly two times lower than that of the dimer S, possibly because the monomer S receives the lost electron to undergo the redox reaction of $S_2^{2-} \rightarrow S^{2-}$ (S_M) + S^0, suggesting the valence state of the S monomer has changed from −1 (bulk) to −2 (defect) with the induced surface vacancies.

4.3. Defect-induced energy offsets in valence band spectra

The intensity, and hence the quantity, of the defective (monomer S) feature in S 2*p* spectra (Fig. 5) increased with sputtering duration and scaled inversely with the content of other S species, indicating the sputtering durations could represent the density of surface vacancies.

Once the formation of the S monomer is complete, it loses its bond to another S, resulting in a single broad S 3*s* band instead of the S 3s σ bonding and σ* antibonding pair in S dimers. This is responsible for the peak intensity increase (except "g") shown in Fig. 7 and the peak disappearance at approximately −15 eV in the DOS spectra (Fig. 9).

To further analyze the difference of the valence band spectra before and after generating defect, differential spectra (Fig. 11) of sputtered and the pristine pyrite {1 0 0} surface are employed and show that the intensity of all peaks, except "g", increased up to a certain degree, suggesting the affected peaks have embedded contributions from the surface defects. As a special case, peak "a" splits into two components (a_1 and a_2) in the differential spectra with only a_1 exhibiting a noticeable increase with defect. On the assumption that S is preferentially removed by Ar^+ during sputtering, this suggests that peak "a_1" represents defective contributions.

The theoretical DOS could explain the change of the valence band spectra. A noticeable feature at the top of valence band in the calculated DOS spectra (Fig. 9) was that the position (0.23 eV) of the outermost peak of both

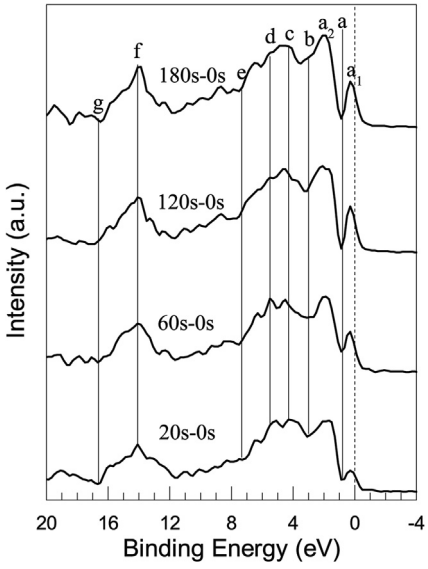

Fig. 11. Differences of XPS valence band spectra between the spectra collected following various durations (20–180 s) of ion sputtering and acid washed pyrite {1 0 0} surface.

5- and 4-coordinated surface defective Fe atoms was significantly closer to the Fermi level (0 eV) in comparison to that (0.32 eV) of the 5-coordinated defective Fe atoms on pristine surfaces. This feature is consistent with peak "a_1" in the differential spectra (Fig. 11), suggesting being one defect state. In conjunction with the sharp emerging peak at 0.32 eV in the DOS of S monomer, this observation suggests the occurrence of Fe-S interactions at defective sites upon developing surface S vacancies, and stronger contributions of S monomers (relative to other S dimers) to the top of the valence band. This feature is consistent with peak "a_2" in the differential spectra (Fig. 11), suggesting as another defect state. Based on these analyses, we can illustrate the energy contribution of various surface and bulk sites, as shown in Fig. 12.

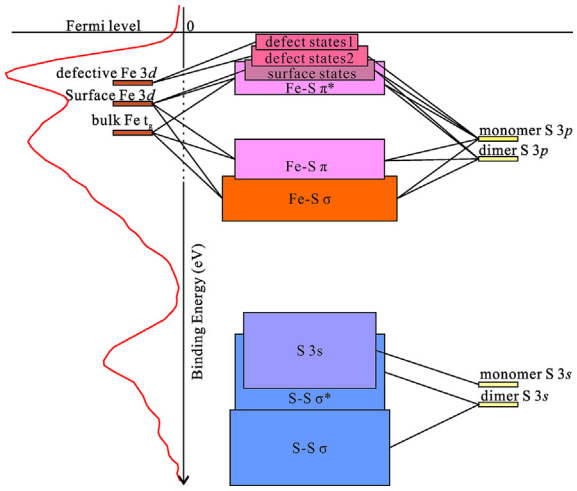

Fig. 12. Valence band model of defective pyrite {1 0 0} surface.

4.4. Valence band offset induced hydroxylation

A direct indication of the energy offsets in valence bands is a promotion of surface reactivity when defects are generated on pristine pyrite surfaces. As illustrated in Fig. 12, the energy of the two defect states of pyrite surfaces are higher than that of the surface state, indicating higher reactivity of defective sites than perfect surface sites. Because the first defect state is contributed from defective Fe only, any reactants close to a defective pyrite surface will first interact with a defective Fe site to lower the energy. Furthermore, the second state will start to work after the interaction between the first defect state and reactants is completed because of its higher energy compared to an intrinsic surface state.

The reactivity promotion by defect states can be directly applied to interpret the defect-induced hydroxylation on pyrite surfaces. When one water molecule interacts with a defective pyrite surface, it first interacts with defect state 1, *i.e.*, adsorption on a defective Fe site. Then the absorbed water molecule interacts with defect state 2, *i.e.*, binding to an S monomer. During the first step, the oxygen first interacts with a defective Fe site, as shown in Fig. 3a. In the second step, the water simultaneously interacts with defective Fe sites and S sites. One hydrogen atom of the water moves toward the S monomer, as shown in Fig. 3b, to lower the energy, which subsequently leads to the water dissociation.

4.5. Generation of hydroxyl radical from pyrite in anaerobic environment

Our results provide fundamental support for the production of hydroxyl radicals in O_2-free water. Although Borda et al. (2003) provide a reasonable assumption of the conversion of Fe(III) to Fe(II) at defect sites, as shown in reaction (1), it appears impossible to oxidate H_2O to $OH^{\cdot}$ directly by the defective Fe(III) due to lacking of a charge difference between the defective and pristine surface Fe atoms in addition to the thermodynamical hindrance (Buckley and Woods, 2015). Based on water dissociation at defective sites and charge distribution as discussed above, we proposed the following pathway to produce hydroxyl radicals in anoxic conditions:

$$2[\equiv Fe(+2.5)] + H_2O + \equiv S \rightarrow 2[\equiv Fe(+2.5)] - OH + \equiv SH \quad (2)$$

$$2[\equiv Fe(+2.5)] - OH \rightarrow 2[\equiv Fe(+2)] + OH^{\cdot} \quad (3)$$

The first step is water dissociation at defective sites; the second step is the formation of $OH^{\bullet}$ and the reduction of defective Fe from +2.5 to +2 states.

In the proposed pathway, reaction (2) is controlled by the concentration of surface defects because of water dissociation only occurs at defective sites. As defects will be exposed at dissolving surfaces, we deduce that the production of $OH^{\bullet}$ from pyrite in O_2-free conditions is controlled by both the defect concentration and dissolution rate.

5. CONCLUDING REMARKS

The development of surface vacancies at S_2^{2-} sites of pyrite surfaces leads to energetically favored water dissociation and the formation of two defect states with higher energy than ordinary surface states. Both defect states are responsible for the energetically favorable water dissociation, *i.e.*, hydroxylation, and ultimately, the generation of $OH^{\cdot}$ on pyrite surfaces. The energetically favorable water dissociation is due to the simultaneously interaction with both defect states. These findings provide insight into the hydroxylation mechanism and, thereby, the $OH^{\cdot}$ generation at the pyrite-water interface in anaerobic environments, which emphasizes the mechanism of hydroxylation on pyrite surfaces. Such a hydroxylation pathway may be a general mechanism for those minerals where water dissociation is energetically unfavorable on their perfect surfaces.

ACKNOWLEDGMENTS

This study is supported by the fund from the Ministry of Science and Technology of the People's Republic of China (2016YFC0600103) and the National Natural Science Foundation of China (Grant Nos. 41573112 and 41702042). This is contribution No. IS-2598 from GIGCAS.

REFERENCES

Abraitis P. K., Pattrick R. A. D. and Vaughan D. J. (2004) Variations in the compositional, textural and electrical properties of natural pyrite: a review. *Int. J. Miner. Process.* **74**, 41–59.

Andersson K. J., Ogasawara H., Nordlund D., Brown G. E. and Nilsson A. (2014) Preparation, structure, and orientation of pyrite FeS_2{100} surfaces: anisotropy, sulfur monomers, dimer vacancies, and a possible FeS surface phase. *J. Phys. Chem. C* **118**, 21896–21903.

Andersson K., Nyberg M., Ogasawara H., Nordlund D., Kendelewicz T., Doyle C. S., Brown G. E., Pettersson L. G. M. and Nilsson A. (2004) Experimental and theoretical characterization of the structure of defects at the pyrite FeS_2(100) surface. *Phys. Rev. B* **70** 195404.

Awramik S. M. (1992) The oldest records of photosynthesis. *Photosynth. Res.* **33**, 75–89.

Bader R. F. (1990) *Atoms in Molecules*. Wiley Online Library.

Blankenship R. E. and Hartman H. (1998) The origin and evolution of oxygenic photosynthesis. *Trends Biochem. Sci.* **23**, 94–97.

Borda M. J., Elsetinow A. R., Schoonen M. A. and Strongin D. R. (2001) Pyrite-Induced Hydrogen peroxide formation as a driving force in the evolution of photosynthetic organisms on an early earth. *Astrobiology* **1**, 283–288.

Borda M. J., Elsetinow A. R., Strongin D. R. and Schoonen M. A. (2003) A mechanism for the production of hydroxyl radical at surface defect sites on pyrite. *Geochim. Cosmochim. Acta* **67**, 935–939.

Buckley A. N. and Woods R. (2015) Can sulfide minerals oxidize water to hydrogen peroxide during grinding in the absence of dissolved oxygen? *Miner. Metall. Process.* **32**, 59–61.

Cabán-Acevedo M., Kaiser N. S., English C. R., Liang D., Thompson B. J., Chen H. E., Czech K. J., Wright J. C., Hamers R. J. and Jin S. (2014) Ionization of high-density deep donor defect states explains the low photovoltage of iron pyrite single crystals. *J. Am. Chem. Soc.* **136**, 17163–17179.

Chen J. H., Long X. H. and Chen Y. (2014) Comparison of multilayer water adsorption on the hydrophobic galena (PbS) and hydrophilic pyrite (FeS_2) surfaces: a DFT study. *J. Phys. Chem. C* **118**, 11657–11665.

Cohn C. A., Borda M. J. and Schoonen M. A. (2004) RNA decomposition by pyrite-induced radicals and possible role of lipids during the emergence of life. *Earth Planet. Sci. Lett.* **225**, 271–278.

Cohn C. A., Fisher S. C., Brownawell B. J. and Schoonen M. A. A. (2010) Adenine oxidation by pyrite-generated hydroxyl radicals. *Geochem. Trans.* **11**, 1–8.

Dos Santos E. C., Silva J. C. D. and Duarte H. A. (2016) Pyrite oxidation mechanism by oxygen in aqueous medium. *J. Phys. Chem. C* **120**, 2760–2768.

Ferrer I. J., Nevskaia D. M., Delasheras C. and Sanchez C. (1990) About the band-gap nature of FeS_2 as determined from optical and photoelectrochemical measurements. *Solid State Commun.* **74**, 913–916.

Garrido-Ramírez E. G., Theng B. K. G. and Mora M. L. (2010) Clays and oxide minerals as catalysts and nanocatalysts in Fenton-like reactions — a review. *Appl. Clay Sci.* **47**, 182–192.

Henkelman G., Arnaldsson A. and Jonsson H. (2006) A fast and robust algorithm for Bader decomposition of charge density. *Comput. Mater. Sci.* **36**, 354–360.

Henkelman G. and Jónsson H. (2000) Improved tangent estimate in the nudged elastic band method for finding minimum energy paths and saddle points. *J. Chem. Phys.* **113**, 9978–9985.

Henkelman G., Uberuaga B. P. and Jónsson H. (2000) A climbing image nudged elastic band method for finding saddle points and minimum energy paths. *J. Chem. Phys.* **113**, 9901–9904.

Herbert F. W., Krishnamoorthy A., Ma W., Van Vliet K. J. and Yildiz B. (2014) Dynamics of point defect formation, clustering and pit initiation on the pyrite surface. *Electrochim. Acta* **127**, 416–426.

Herbert F. W., Krishnamoorthy A., Van Vliet K. J. and Yildiz B. (2013) Quantification of electronic band gap and surface states on FeS_2(100). *Surf. Sci.* **618**, 53–61.

Javadi Nooshabadi A. and Hanumantha Rao K. (2014) Formation of hydrogen peroxide by sulphide minerals. *Hydrometallurgy* **141**, 82–88.

Javadi Nooshabadi A., Larsson A.-C. and Kota H. R. (2013) Formation of hydrogen peroxide by pyrite and its influence on flotation. *Miner. Eng.* **49**, 128–134.

Kasting J. F. and Pollack J. B. (1984) Effects of high CO_2 levels on surface temperature and atmospheric oxidation state of the early Earth. *J. Atmos. Chem.* **1**, 403–428.

Kasting J. F., Zahnle K. J., Pinto J. P. and Young A. T. (1989) Sulfur, ultraviolet radiation, and the early evolution of life.. *Orig. Life Evol. Biosphere J. Int. Soc. Study Orig. Life* **19**, 95–108.

Kleppe A. K. and Jephcoat A. P. (2004) High-pressure Raman spectroscopic studies of FeS_2 pyrite. *Mineral. Mag.* **68**, 433–441.

Kresse G. and Furthmuller J. (1996) Efficiency of ab-initio total energy calculations for metals and semiconductors using a plane-wave basis set. *Comput. Mater. Sci.* **6**, 15–50.

Kresse G. and Joubert D. (1999) From ultrasoft pseudopotentials to the projector augmented-wave method. *Phys. Rev. B* **59**, 1758–1775.

Kwan W. P. and Voelker B. M. (2003) Rates of hydroxyl radical generation and organic compound oxidation in mineral-catalyzed fenton-like systems. *Environ. Sci. Technol.* **37**, 1150–1158.

McKay C. P. and Hartman H. (1991) Hydrogen peroxide and the evolution of oxygenic photosynthesis. *Orig. Life Evol. Biosphere J. Int. Soc. Study Orig. Life* **21**, 157–163.

Monkhorst H. J. and Pack J. D. (1976) Special points for Brillouin-zone integrations. *Phys. Rev. B* **13**, 5188–5192.

Momma K. and Izumi F. (2008) VESTA: a three-dimensional visualization system for electronic and structural analysis. *J. Appl. Crystallogr.* **41**, 653–658.

Nesbitt H., Bancroft G., Pratt A. and Scaini M. (1998) Sulfur and iron surface states on fractured pyrite surfaces. *Am. Mineral.* **83**, 1067–1076.

Nesbitt H. W., Scaini M., Hochst H., Bancroft G. M., Schaufuss A. G. and Szargan R. (2000) Synchrotron XPS evidence for Fe^{2+}-S and Fe^{3+}-S surface species on pyrite fracture-surfaces, and their 3D electronic states. *Am. Mineral.* **85**, 850–857.

Nesbitt H. W., Uhlig I., Bancroft G. M. and Szargan R. (2003) Resonant XPS study of the pyrite valence band with implications for molecular orbital contributions. *Am. Mineral.* **88**, 1279–1286.

Perdew J. P., Burke K. and Ernzerhof M. (1996) Generalized gradient approximation made simple. *Phys. Rev. Lett.* **77**, 3865–3868.

Raebiger H., Lany S. and Zunger A. (2008) Charge self-regulation upon changing the oxidation state of transition metals in insulators. *Nature* **453**, 763–766.

Sanville E., Kenny S. D., Smith R. and Henkelman G. (2007) Improved grid-based algorithm for Bader charge allocation. *J. Comput. Chem.* **28**, 899–908.

Schaufuss A. G., Nesbitt H. W., Kartio I., Laajalehto K., Bancroft G. M. and Szargan R. (1998) Reactivity of surface chemical states on fractured pyrite. *Surf. Sci.* **411**, 321–328.

Schoonen M., Smirnov A. and Cohn C. (2004) A Perspective on the role of minerals in prebiotic synthesis. *AMBIO J. Hum. Environ.* **33**, 539–551.

Shirley D. A. (1972) High-resolution X-ray photoemission spectrum of the valence bands of gold. *Phys. Rev. B* **5**, 4709.

Sit P. H. L., Cohen M. H. and Selloni A. (2012) Interaction of oxygen and water with the (100) surface of pyrite: mechanism of sulfur oxidation. *J. Phys. Chem. Lett.* **3**, 2409–2414.

Stevens E. D., Delucia M. L. and Coppens P. (1980) Experimental-observation of the effect of crystal-field splitting on the electron-density distribution of iron pyrite. *Inorg. Chem.* **19**, 813–820.

Stirling A., Bernasconi M. and Parrinello M. (2003) Ab initio simulation of water interaction with the (100) surface of pyrite. *J. Chem. Phys.* **118**, 8917.

Stirling A., Bernasconi M. and Parrinello M. (2007) Defective pyrite (100) surface: an ab initio study. *Phys. Rev. B* **75** 165406.

Tang W., Sanville E. and Henkelman G. (2009) A grid-based Bader analysis algorithm without lattice bias. *J. Phys. Condens. Matter* **21** 084204.

Tian F., Toon O. B., Pavlov A. A. and Sterck H. D. (2005) A hydrogen-rich early earth atmosphere. *Science* **308**, 1014–1017.

Wang W., Qu Y., Yang B., Liu X. and Su W. (2012) Lactate oxidation in pyrite suspension: a Fenton-like process in situ generating H_2O_2. *Chemosphere* **86**, 376–382.

Yeh J. J. and Lindau I. (1985) Atomic subshell photoionization cross-sections and asymmetry parameters. *At. Data Nucl. Data Tables* **32**, 1–155.

Zhang P., Yuan S. and Liao P. (2016) Mechanisms of hydroxyl radical production from abiotic oxidation of pyrite under acidic conditions. *Geochim. Cosmochim. Acta* **172**, 444–457.

Zhang Y. N., Hu J., Law M. and Wu R. Q. (2012) Effect of surface stoichiometry on the band gap of the pyrite FeS_2(100) surface. *Phys. Rev. B* **85** 085314.

Zhang Y. N., Law M. and Wu R. Q. (2015) Atomistic modeling of sulfur vacancy diffusion near iron pyrite surfaces. *J. Phys. Chem. C* **119**, 24859–24864.

Associate editor: Jean-francois boily